

Control and Pointing Challenges of Large Antennas and Telescopes

Wodek Gawronski

Abstract—Extremely large telescopes will be constructed in the near future, and new radiotelescopes will operate at considerably higher radio frequencies; both features create significantly increased pointing accuracy requirements that have to be addressed by control system engineers. This paper presents control and pointing problems encountered during design, testing, and the operation of antennas, radiotelescopes, and optical telescopes. This collection of challenges informs of their current status, helps to evaluate their importance, and is a basis for discussion on the ways of improvement of antenna pointing accuracy.

Index Terms—Antenna mechanical factors, antenna transient analysis, antennas, control engineering, control systems, linear-quadratic-Gaussian control, tracking.

I. INTRODUCTION

THIS PAPER presents pointing and control problems typically encountered during the design of new antennas, radiotelescopes, and optical telescopes. Radiotelescopes receive signals at radiofrequencies lower than optical telescopes. They use parabolic dishes rather than mirrors. The dish size is larger (up to 100 m) than mirrors of optical telescopes (up to 10 m). Antennas/telescopes need to track at various rates, mostly at the sidereal rate ($4.2 \text{ m}^\circ/\text{s}$)—to take out the Earth rotation. Thus, moving a large antenna accurately is a more challenging task than holding it fixed. Antennas, like radiotelescopes, receive radiofrequency signals, but unlike the latter, also send them. The antennas are used for spacecraft communication.

The newly designed antennas, radiotelescopes and telescopes have to satisfy control and pointing requirements that challenge existing technology. In order to increase the data rate, the antennas are required to communicate at higher radiofrequencies: from *S*-band (2.5 GHz), to *X*-band, (8.5 GHz), to *Ka*-band (32 GHz). The increased frequency requires more precise pointing: 28 m° for *S*-band, 8 m° for *X*-band, and 2 m° for *Ka*-band. The telescope size also increases, from a 12-m Keck telescope to 30- or 50-m future telescopes which are now on drawing boards. The increased size creates multiple pointing and control challenges.

Manuscript received August 27, 2004; revised March 11, 2005. Manuscript received in final form September 21, 2006. Recommended by Associate Editor S. Devasia. This work was supported in part by the National Aeronautics and Space Administration under a contract.

The author is with the Jet Propulsion Laboratory, California Institute of Technology, Pasadena, CA 91109 USA (e-mail: wodek.k.gawronski@jpl.nasa.gov).

Color versions of Figs. 1, 2, 4–9, 11–13, 15, 16, 19–22, 24–27, and 29–31 are available online at <http://ieeexplore.ieee.org>.

Digital Object Identifier 10.1109/TCST.2006.886434

This paper is based predominantly on my experience with the NASA Deep Space Network, although other experience is included in the references. Obviously, there are too many references to be included in this short review, but readers interested in further study of antenna and telescope control and pointing issues are referred to the *IEEE Antenna and Propagation Magazine*, *Proceedings of SPIE* (the International Society for Optical Engineering), *Optical Engineering (SPIE Journal)*, and the *Interplanetary Network Progress Report (JPL)*, [1]. There are three books, that address antenna pointing and control issues, [2]–[4], and my book [5], although it addresses general issues of structural dynamics and control, it also includes many examples of antenna dynamics and antenna control systems. General antenna theory is presented in a comprehensible form in [6] and [7].

II. ANTENNA AND TELESCOPE EXAMPLES

A. NASA Deep Space Network

The NASA Deep Space Network (DSN) antennas communicate with spacecraft by sending commands (uplink) and by receiving information from spacecraft (downlink). To assure continuous tracking during Earth's rotation, the antennas are located at three sites: at Goldstone, CA, Madrid, Spain, and Canberra, Australia. The signal frequencies are 8.5 GHz (*X*-band) and 32 GHz (*Ka*-band). The dish size of the antennas is either 34 or 70 m. An example of the 70-m antenna is shown in Fig. 1. The antenna dish rotates with respect to the horizontal (or elevation) axis. The whole antenna structure rotates on a circular track (azimuth track) with respect to the vertical (or azimuth) axis. For the *Ka*-band frequency, the required tracking accuracy is on the order of 1 m° . This requirement is a driver for the control system upgrade of the antennas. In [5] and [8], one can find the description of the DSN antenna control systems, and at the webpage listed in [1], one may find the DSN antennas research reports, including control systems. The Deep Space Network webpage is at [9].

B. Large Millimeter Telescope

The Large Millimeter Telescope (LMT) project is the joint effort of the University of Massachusetts at Amherst and the Instituto Nacional de Astrofísica, Óptica, y Electrónica (INAOE) in Mexico. The LMT is a 50-m diameter, radio-telescope, designed for principal operation at wavelengths between 1 and 4 mm. The telescope rotates with respect to elevation and azimuth axes. It is being built atop Sierra Negra (4640 m), a volcanic peak in

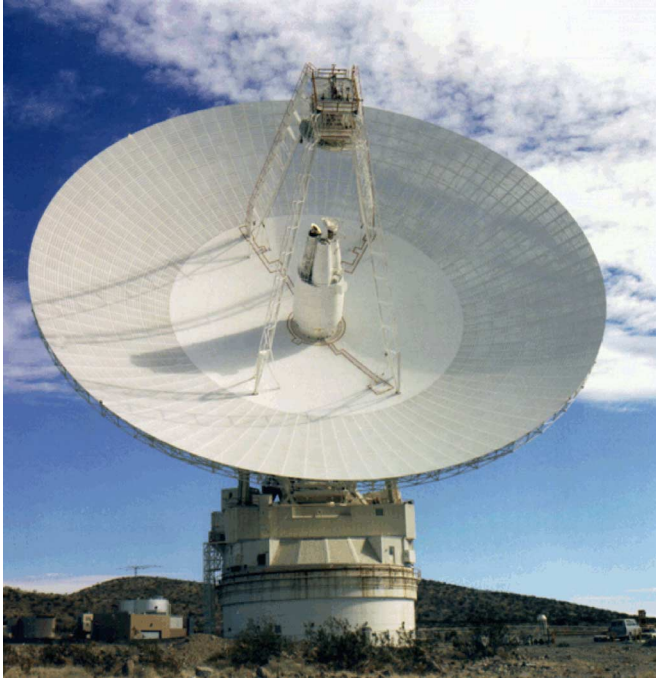


Fig. 1. NASA/JPL 70-m antenna at Goldstone, CA (courtesy of NASA/JPL/Caltech, Pasadena, CA).

the state of Puebla, Mexico. The telescope construction is expected to be complete in 2006. The LMT will be a significant step forward in antenna design. In order to reach its pointing accuracy specifications, it must outperform every other telescope in its frequency range. The antenna designer expects that the telescope will point to its specified accuracy of 0.3 m° under conditions of low winds and stable temperatures, with radio frequencies up to 110 GHz. For more about LMT, see [10].

C. APEX Telescope

The Max Planck Institute for Radioastronomy installed the 12-m Atacama Pathfinder Experiment (APEX) telescope in the Chilean Atacama desert at Llano de Chajnantor at a 5000-m altitude, see [11]. This telescope will be used for observations in the submillimeter wavelength range. The overall surface accuracy of $20 \text{ }\mu\text{m}$ and the pointing accuracy of 0.16 m° have been proven during acceptance testing carried out in 2004.

D. ESA Deep Space Antennas

For use in deep space, high elliptical orbit missions, and future missions to Mars, the European Space Agency (ESA) procured 35-m deep space ground stations, see [12]. The antennas are designed for frequencies up to 35 GHz and a pointing accuracy of 6 m° . The first antenna (that moves in azimuth and elevation axes) has been installed in Australia and has proven its compliance to the specifications. The second antenna is under construction in Spain. The 35-m antenna incorporates a full motion pedestal with a beam waveguide system.

E. ALMA Prototype

The Atacama Large Millimeter Array (ALMA) is an international astronomy facility. A brief description can be found

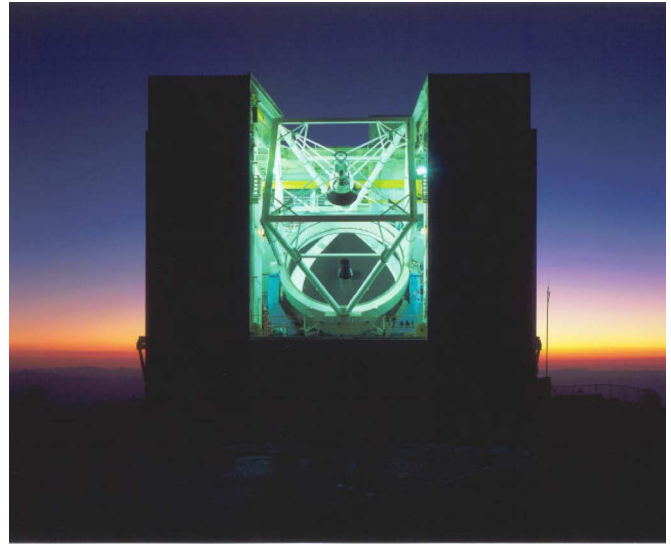


Fig. 2. MMT at sunset. Photo by H. Lester.

at [13]. The pointing accuracy of the 12-m ALMA telescope is 0.16 m° . The control system must handle very accurate movement at sidereal tracking velocities as well as several extremely fast switching functions. To do this, the drives are designed to accelerate up to $24 \text{ }^\circ/\text{s}^2$, which is very unusual for a telescope of this size.

F. Thirty-Meter Telescope

The thirty-meter telescope (TMT) will be the first of the giant optical/infrared ground-based telescopes (of 30-m diameter of primary mirror) addressing the compelling areas in astrophysics: the nature of dark matter, the assembly of galaxies, the growth of structure in the Universe, and the physical processes involved in star and planet formation. TMT will operate over $0.3\text{--}30\text{-}\mu\text{m}$ wavelength range, providing 9 times the collecting area of the current largest optical telescope, the 10-m Keck Telescope. It will use the adaptive optics system to allow diffraction-limited performance, resulting in spatial resolution 12.5 times sharper than is achieved by the Hubble Space Telescope. For more about TMT, see [14].

G. Multiple Mirror Telescope

The multiple mirror telescope (MMT) (see Fig. 2) is a joint project of the University of Arizona and the Smithsonian Institution. Located on Mt. Hopkins, AZ, the MMT is a 6.5-m optical telescope used for spectroscopy, wide-field imaging, and adaptive optics astronomy.

Several advances in telescope design were pioneered at the MMT. Among these: compact, altitude-azimuth structure with corotating building, *in situ* aluminization of the primary mirror, and adaptive optics with deformable secondary mirrors and artificial guide stars.

The MMT was first designed as a multiple-mirror telescope, with six 1.8-m primary mirrors in a single mount. Automated alignment of the individual light paths gave the telescope an

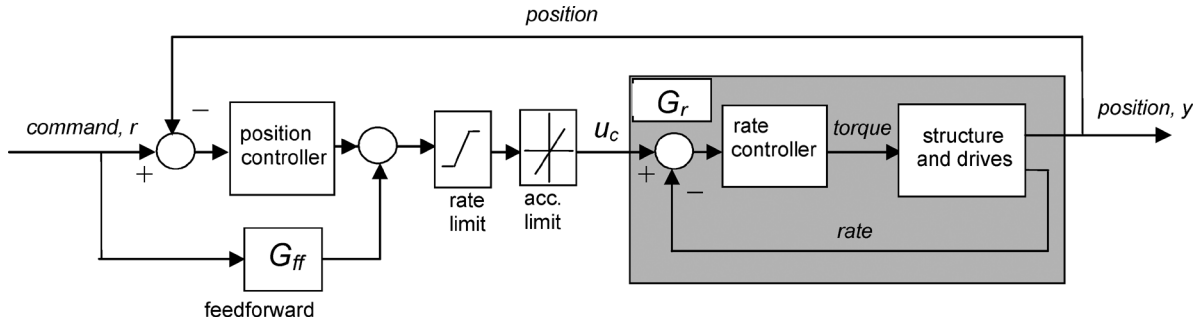


Fig. 3. Antenna control system: G_r , antenna with the rate loop and G_{ff} feedforward loop, r command, y position, and u_c rate command.

equivalent aperture of 4.5 m, with a 6.9-m baseline for interferometry. The recent upgrade created a new 6.5-m class telescope. The MMT webpage can be found at [15].

III. CONTROL SYSTEM STRUCTURE

A typical antenna is moved in azimuth (vertical) axis and elevation (horizontal) axis. The movements are independent, and their control systems are independent as well. Due to the independence, in the following we will consider a single axis only.

An antenna control system consists of the rate and position feedback loops, as shown in Fig. 3. The rate loop includes antenna structure and the drives. The drive (motor) rate is fed back to the rate controller. Typically, the rate loop is designed such that the antenna steady-state rate is proportional to the constant rate-loop input, i.e., it acts as an integrator; and therefore, the rate-loop input is called the rate command. The antenna position is measured with the azimuth and elevations encoders. The position loop is an outer loop that feeds back the antenna position.

The antenna rate and acceleration are limited (see Fig. 3) and the limits reflect the restricted power of the antenna drives. During tracking, the limits are not violated, however, the rate and acceleration limits are hit during antenna slewing.

IV. CONTROL SYSTEM MODELS

Antenna control system models are indispensable in the antenna controller design and implementation stages for two reasons. In the design stage, they are used to determine the controller gains and to assess the control system performance; in the implementation stage the models are part of antenna controllers, and help to fine-tune the antenna pointing precision.

In the design stage, an analytical model of the control system is developed. It includes the finite-element model of structure, motor, and gearbox models, amplifiers and filters, and also nonlinearities: friction, backlash, rate, and acceleration limits. An example of such a model is given in [16] and [17] and a drive system model in [18] and [19].

In the implementation stage, the antenna model is obtained from the open-loop antenna field tests using a system identification procedure. The model accuracy is particularly important when the antenna controller is a model-based controller, such as a LQG or a H_∞ controller.

In order to obtain the model, an antenna is excited with the white noise (a noise is “white” if its bandwidth is much

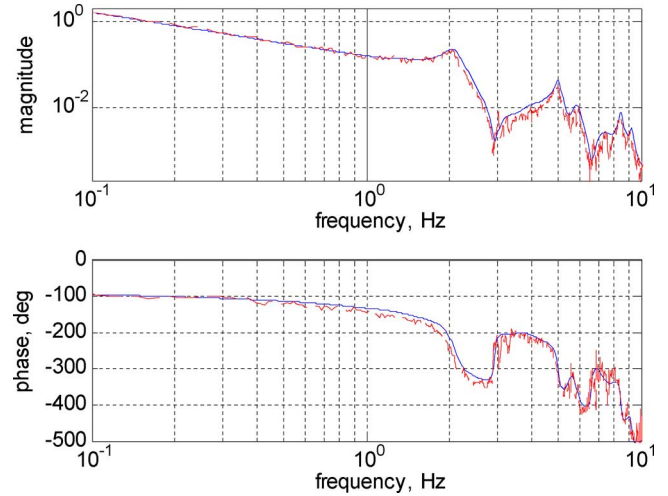


Fig. 4. Transfer function of 34-m DSN antenna, azimuth axis, from (dashed line) field data and from (solid line) identification: (a) magnitude and (b) phase.

wider than the bandwidth of the open-loop antenna), and the encoder output is recorded. From the input and output records, the transfer function is obtained [5], [20] and the example of the azimuth transfer function of the 34-m antenna is shown in Fig. 4 (dashed line). From the input-output (I/O) data the system state-space model is identified. In Fig. 4, the magnitude of the transfer function obtained from the identified state-space model is shown as a solid line. The magnitude of the transfer function consists of the rigid body part that dominates lower frequencies (below 1 Hz), and is characterized with the -20 dB/d slope. At higher frequencies—above 1 Hz—the transfer function shows flexible deformations characterized by resonant peaks. The development of the control system based on the identified model can be found in [5] and [21]; on a telescope identification using swept-sine generator, see [22]; on Galileo Telescope model identification, see [23].

The antenna azimuth model depends on the antenna elevation position. Note, for example, that an antenna with its dish at zenith has different structural properties than the antenna with its dish pointed horizontally. Fig. 5 shows the measured magnitudes of the azimuth transfer functions for a 34-m antenna at different elevation positions. The variations of the first two natural frequencies with respect to the antenna elevation position are shown in Fig. 6. From these figures, we see that the natural frequencies depend on the antenna elevation position; the second frequency changes significantly with the elevation angle.

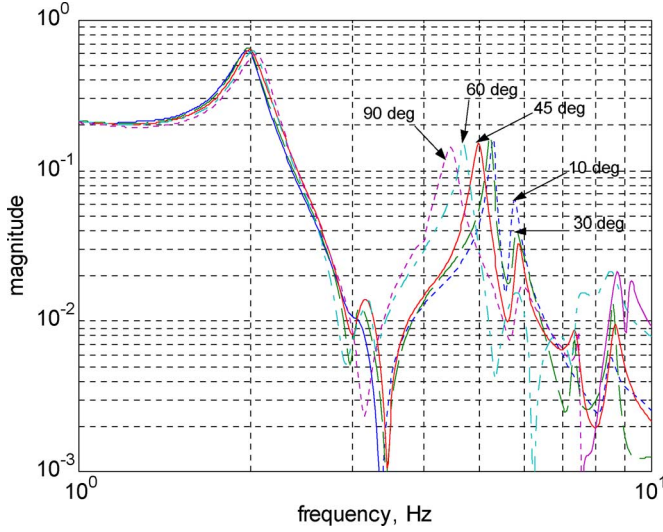


Fig. 5. Magnitude of the azimuth transfer function of 34-m DSN antenna for different elevation angles.

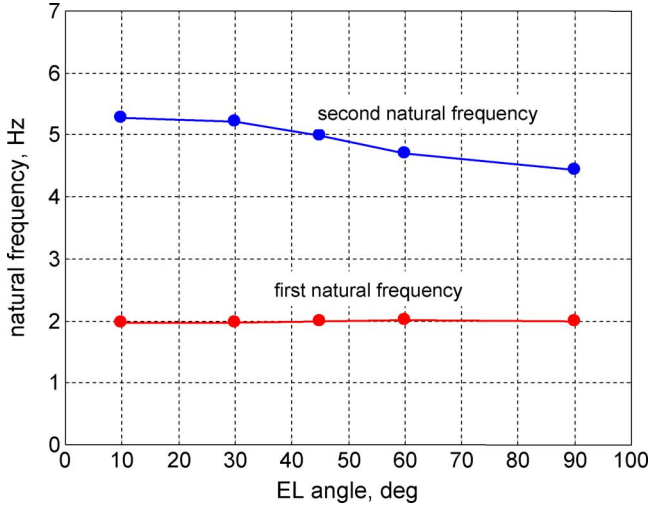


Fig. 6. Variation of the first two natural frequencies of the antenna structure as a function of its elevation position.

An antenna's natural frequencies depend also on the antenna size. It is a general tendency that the natural frequencies decrease with the increase of the antenna size (the structure becomes “softer”). The lowest natural frequency (called the fundamental frequency) is considered a measure of compliance of a structure. The Aerospace Corporation collected data of fundamental frequencies of many antenna structures. In these data, the decreasing tendency of frequencies with the increase of antenna dish size is observed. Based on these data, we determined the best fit line defined by the following equation:

$$f = 20.0d^{-0.7}. \quad (1)$$

The line (in logarithmic scale) is presented in Fig. 7. In the previous equation, d is antenna diameter in meters and f is the antenna fundamental (lowest) frequency in Hz. This equation represents the average natural frequency for a given antenna diameter. Equation (1) allows evaluating the structural soundness

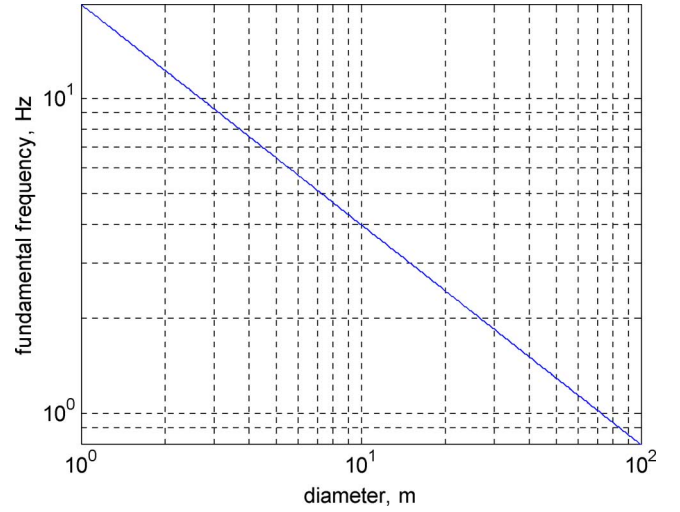


Fig. 7. Best fit line that fits the Aerospace Corporation chart of the antenna fundamental frequencies.

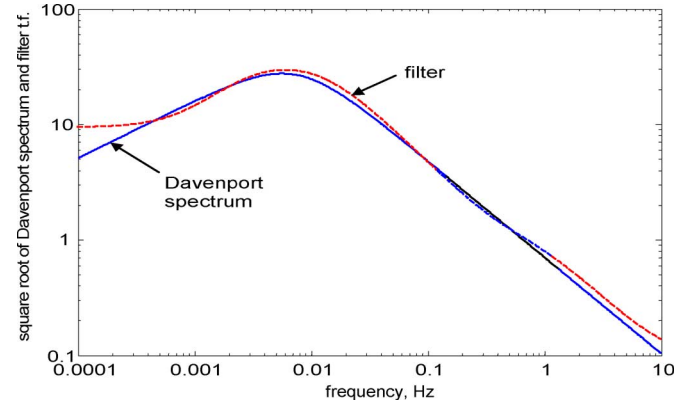


Fig. 8. Davenport spectrum and its approximating filter.

of a particular antenna. If the fundamental frequency of the considered antenna structure is higher than the frequency obtained from (1), the structure is stiffer than the average (thus, of better pointing performance), if it is lower—the structure is softer than average (thus, of inferior pointing performance).

V. DISTURBANCE MODEL

The antenna's main disturbance is wind. Wind gusts spectra depend on the geographical location and the terrain profile. Different spectra, based on wind gusts measurements, are used to model wind gusts. We present here the Davenport spectrum $S_v(\omega)$ that depends on average wind speed and terrain roughness as follows [24]:

$$S_v(\omega) = 4800v_m\kappa \frac{\beta\omega}{(1 + \beta^2\omega^2)^{\frac{4}{3}}} \quad (2)$$

where v_m is the mean wind speed, $\beta = 600/\pi v_m$, and κ is the surface drag coefficient, obtained from the roughness of the terrain, see [25], $\kappa = (2.5 \ln(z/z_o))^{-2}$. In the previous equation, z is the distance from the ground to the antenna dish center and z_o is the height of the terrain roughness (e.g., $z_o = 0.1$ to 0.3 m at Goldstone, CA). For 34-m antennas $z = 17$ m, thus, $\kappa = 0.006$ to 0.010 . The Davenport spectrum is shown in Fig. 8 (solid line).

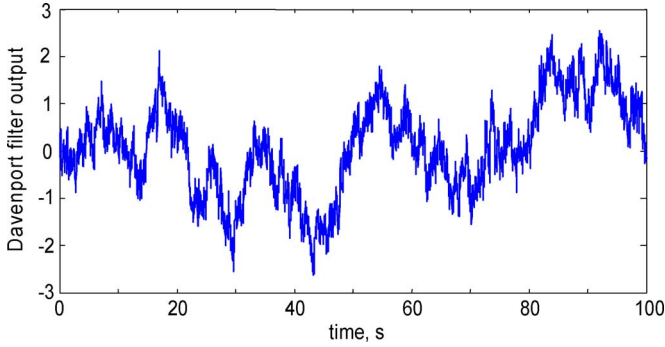
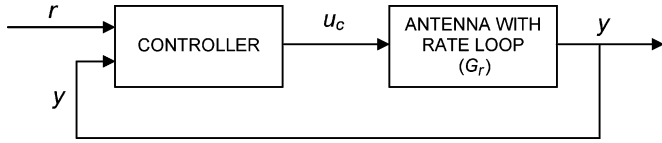


Fig. 9. Wind gust time history obtained from the Davenport filter.

Fig. 10. Position controller of an antenna: r command, u_c rate command, and y encoder.

In order to model wind gusts velocity $\Delta v(t)$ in time domain, the spectrum is approximated with a linear filter. The filter was obtained in [26], by adjusting the filter parameters, such that the magnitude of the filter transfer function best fits the Davenport spectrum within the antenna bandwidth of [0.001, 20] Hz. The resulting digital filter transfer function is for the sampling time of 0.02 s is as follows:

$$G_w = \frac{0.1584z^3 - 0.3765z^2 + 0.2716z - 0.0534}{z^4 - 2.9951z^3 + 3.0893z^2 - 1.1930z + 0.0988}. \quad (3)$$

The gust velocity $\Delta v(t)$ is obtained as an output of the filter excited with a white noise of unit variance. The plot of the magnitude of the filter transfer function is shown in Fig. 8. A sample of the wind speed generated by the filter is shown in Fig. 9.

Having wind speed, the wind force is obtained (in Newtons) as follows:

$$F_w(t) = k_f \Delta v(t) \quad (4)$$

where the coefficient k_f depends on the roughness of the terrain and the mean wind speed v_m m/s, $k_f = 0.000892v_m^2$, see [27], and $\Delta v(t)$ is the wind gust velocity, obtained from the Davenport spectrum. On the Gemini Telescope wind model see [28], on steady-state wind modeling see [29], and on wind simulations see [30].

VI. POSITION CONTROLLERS

We present an antenna performance with PI, feedforward, LQG, and H_∞ position controllers. On the application of predictive controller to antenna control, see [31]; on periodic disturbance rejection see [32].

A. Antenna Performance With PI Controller

Consider the proportional (P) and integral (I) actions independently. Its location in the antenna control system is shown in the block diagram in Fig. 10, where “antenna” denotes the antenna structure and drives with closed-rate loop, cf. Fig. 3.

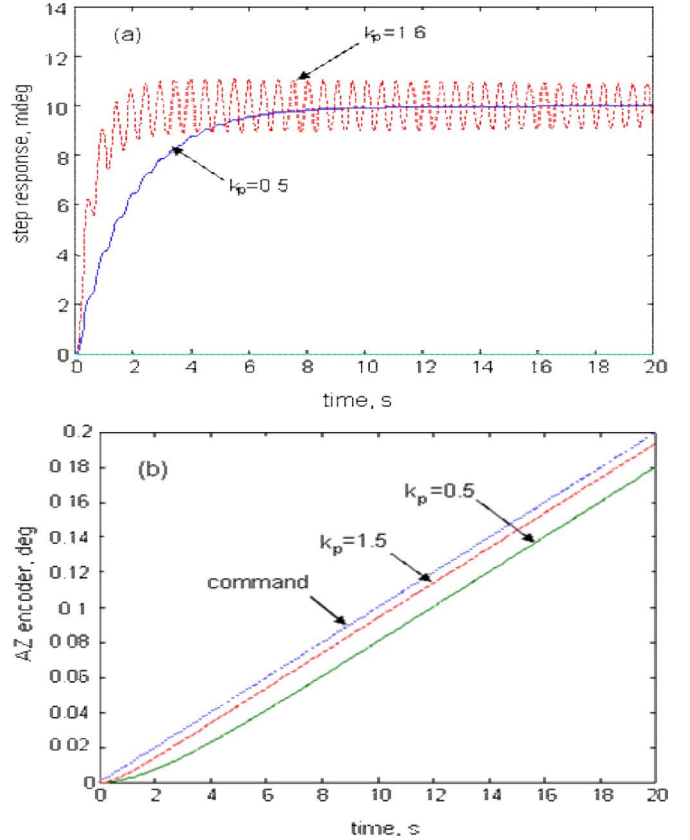


Fig. 11. Limits of performance of the proportional controller: (a) step responses and (b) rate offset responses.

Assuming a zero integral gain $k_i = 0$ and the proportional gain $k_p = 0.5$, the response of the closed-loop system to a 10-m° step command is shown in Fig. 11(a) (solid line). It has no overshoot and a settling time is 7 s. The response to 10 m°/s rate offset has constant servo error (or lagging) of 20 m°, see Fig. 11(b). The lag can be reduced by increasing the proportional gain. Indeed, increasing the gain to 1.5 produces 6 m° lag; note, however, that the system is almost unstable [see the step response in Fig. 11(a)]. Thus, the proportional controller cannot completely eliminate the lagging.

The integral gain eliminates the lagging, however, a servo error in the antenna response to the 10 m°/s rate offset (with proportional gain $k_p = 0.5$ and integral gain $k_i = 0.1$) is shown in Fig. 12(b). Indeed, the rate-offset response has zero steady-state error, as a result of the action of the integrator (for non-zero steady-state error the integral of the error grows indefinitely causing strong controller action). On the other hand, the integrator of the PI controller produces an overshoot, see Fig. 12(a).

The response of the PI controller to 10 m°/s disturbance step [pictured in Fig. 12(b)] is slow and of large amplitude. The servo error in 10 m/s wind gusts is quite large: 1.6 m°, see Table I. The variable structure PI controller was described in [33].

B. Antenna Performance With Feedforward Controller

The feedforward loop is added to improve its tracking accuracy at high rates [8]. In this loop, the command is differenti-

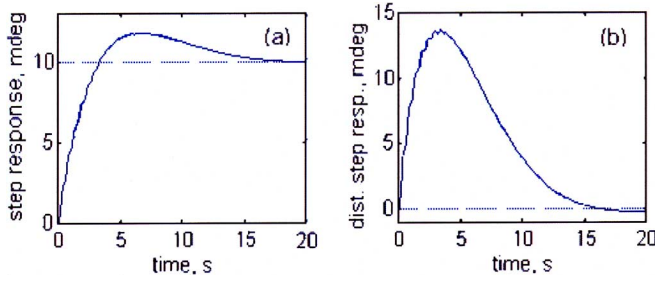


Fig. 12. Antenna performance with the PI controller.

TABLE I
RMS SERVO ERROR IN 10 m/s WIND GUSTS

Controller	AZ servo error (mdeg)	EL servo error (mdeg)
PI	0.5 [#]	1.6 [#]
LQG	0.03	0.11
H _∞	0.02	0.05

[#] from measurements, see [34].

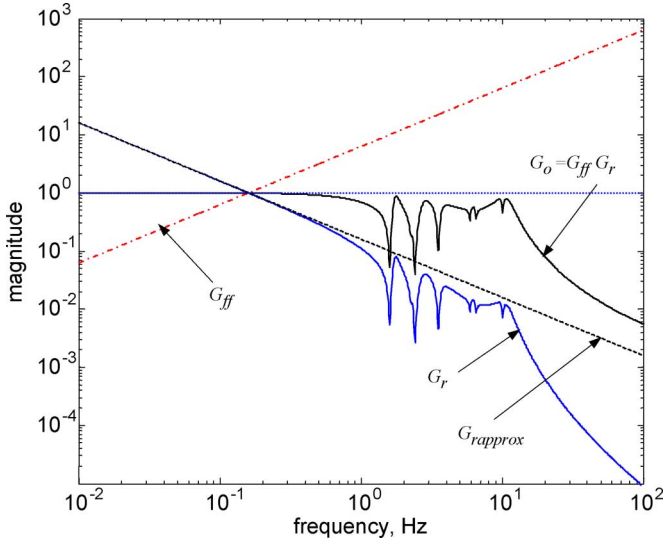


Fig. 13. Feedforward action is illustrated with the magnitudes of the transfer functions (G_r is the rate-loop transfer function, G_{rapprox} is the rate-loop transfer function approximation, G_{ff} is the feedforward loop transfer function, and $G_o = G_{\text{ff}}G_r$ is the transfer function of the series connection of feedforward and rate-loops).

ated and forwarded to the rate-loop input, see Fig. 3. The rate loop transfer function can be approximated with an integrator, see Fig. 13, thus, a derivative is an approximation of the inverse of the rate loop transfer function. In this way we obtain the open-loop transfer function from the command to the encoder approximately equal to 1. Indeed, the magnitude of the rate-loop transfer function G_r is shown in Fig. 13. It is approximated (up to 1 Hz) with an integrator ($G_{\text{rapprox}} = 1/s$), shown in the same figure (dashed line). The feedforward transfer function is a derivative ($G_{\text{ff}} = s$) shown in Fig. 13, (dash-dotted line), so that the overall open-loop transfer function is a series of the feedforward and the rate loop $G_o = G_r G_{\text{ff}}$, which is approximately equal to 1 up to the frequency 1 Hz. The position feedback is added to compensate disturbances and system imperfections.

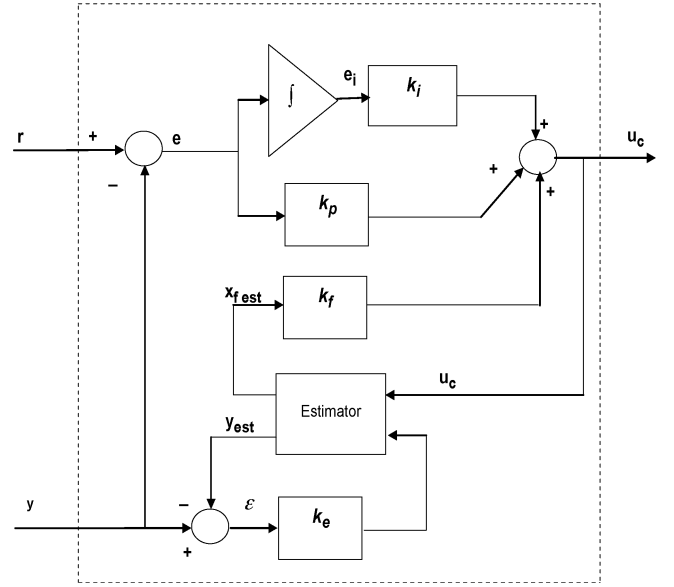


Fig. 14. LQG controller structure.

C. Antenna Performance With LQG Controller

It has been noted that the bandwidth, the speed of the system response, and the disturbance suppression abilities of the PI controller improve with the increase of the controller proportional gain (up to a limiting value at which the fundamental mode becomes unstable). If the vibrations could be sensed and suppressed, then the performance of the antenna control system could be further improved.

The encoder is the antenna position sensor. The Fourier transformation of the encoder measurements show antenna vibrations, indicating that the antenna vibrations are present in the measurements, and can be recovered from the encoder data. Using the same controller diagram as in Fig. 10, the PI controller is replaced with a controller as in Fig. 14. This controller uses an estimator. The estimator is a software model of the antenna. It is driven by the same input as the antenna, and by the estimation error (the difference between the actual encoder reading and the estimated encoder reading). The error is amplified with the estimator gain k_e to correct for transient dynamics, see Fig. 14.

The estimator returns the antenna states that consist of the estimated encoder reading (or noise free encoder measurements), and the estimated states x_f of the flexible deformations of the antenna structure. The latter states effectively replace the missing vibration measurements. The resulting controller's output is a combination of the PI controller outputs and the flexible mode controller output. The first takes care of the tracking motion, the latter suppresses the antenna vibrations. In the previous configuration, the increased P and I gains do not destabilize the closed-loop system, since the flexible-mode controller keeps the antenna vibrations suppressed.

If the gains are determined such that the so called LQG index is minimized, the resulting controller is an LQG controller. The description of the LQG controller design one can find in [5], [20], and [35], and a design tool is described in [36]. The application of the LQG controller to a 20-m radiotelescope is described in [37].

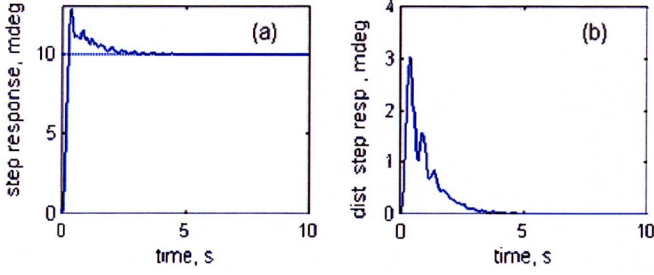
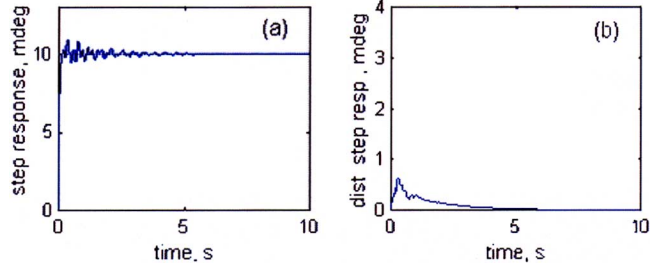


Fig. 15. Antenna performance with LQG controller.

Fig. 16. Antenna performance with H_∞ controller.

The performance of the LQG controller designed for a 34-m antenna is illustrated in Fig. 15(a) (the response to a 10° step command), and in Fig. 15(b) (the response to $10^\circ/\text{s}$ disturbance step). The step response has a small settling time of 2 s, and the disturbance step response has a low magnitude of short duration (2 s). The rate offset shows zero lagging. The servo error in 10 m/s wind gusts is small: 0.03° (Table I). The settling time and the servo error in wind of the LQG controller are of an order smaller than those of the PI controller.

D. Antenna Performance With H_∞ Controller

The H_∞ controllers outperform LQG controllers in many applications. The structure of an H_∞ controller is similar to that of the LQG controller, but its parameters are obtained from a different algorithm, while the LQG controller minimizes the system H_2 norm (its RMS response to the white noise input), the H_∞ controller algorithm minimizes the system H_∞ norm (in case of a single-input single-output system, the system H_∞ norm is the maximal magnitude of its transfer function).

The antenna H_∞ controller was designed by shaping the disturbance input. A filter of the Davenport wind spectrum profile was used as a shaping (or weighting) factor. The H_∞ controller design for antenna tracking purposes is described in [5] and [38]. The performance of the antenna is shown in Fig. 16. The figures show very small settling time (1.2 s) and small overshoot (less than 10%). These features significantly exceed LQG controller performance. (However, one should note that this comparison is not fair; the LQG results present an implemented controller, where many factors forced the degradation of its performance, while the H_∞ controller performance represents the simulated results only.) The response to the $10^\circ/\text{s}$ rate offset has zero steady-state error. The servo error in 10 m/s wind gusts is small: 0.02° , see Table I.

The application of the H_∞ controller to the airborne telescope SOFIA is described in [39], for Thirty Meter Telescope in [40],

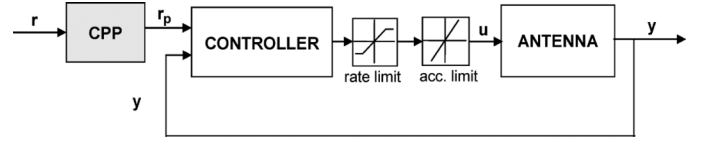


Fig. 17. CPP location in the antenna control system.

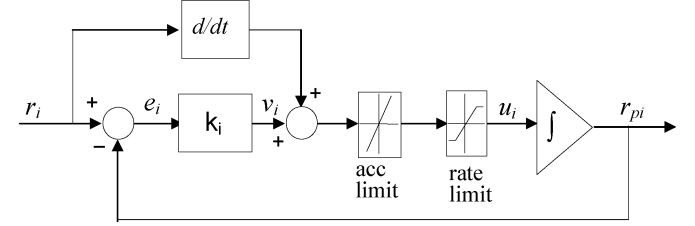


Fig. 18. CPP block diagram.

to a segmented mirror telescope in [41] and [42], and to the secondary mirror of a Giant Segmented Mirror Telescope in [43].

VII. COMMAND PREPROCESSOR

When LQG or H_∞ controller is implemented, it causes limit cycling during antenna slewing operations. This phenomenon is caused by the antenna rate and acceleration limits: the controllers are designed for a linear plant, while limits induce antenna nonlinear dynamics. In order to avoid the cycling, one can either apply different controllers for tracking and for slewing; or implement an anti-windup technique, see [44]; or apply a controller with variable gains [33], [45]; or use a trajectory calculated in advance, such that it never exceeds the rate and acceleration limits [46]; or use a command preprocessor (CPP), see [25]. This paper presents the latter approach. The preprocessor is an algorithm that generates a modified command, identical with the original one, if the rate and accelerations are within the limits; and a command of (almost) maximal or minimal rate and acceleration, when the limits are met or violated. The location of the preprocessor in the antenna control system is shown in Fig. 17.

The block diagram of the CPP is shown in Fig. 18. It imitates a rigid antenna (represented by the integrator) driven by a variable-gain controller with a feedforward gain (the latter represented by the derivative). The variable gain k_i depends on the preprocessor error e_i as follows:

$$k_i = k_o + k_v e^{-\beta|e_i|}. \quad (5)$$

In this equation, k_o is the constant part of the gain, k_v is the variable part of the gain, and β is the error exponential. The plot of $k_i(e_i)$ for $k_o = 1$, $k_v = 5$, and $\beta = 20$ is shown in Fig. 19. The detail description of CPP is given in [25].

The CPP response to the step of 10° is shown in Fig. 20. The preprocessed command begins with the maximal acceleration until it reaches the maximum rate, then continues with the maximal (and constant) rate and, finally, slows-down with the maximal deceleration. After reaching the value of 10° , the error between the original and the preprocessed command is zero.

The measured responses of the antenna to a large (nonprocessed) step input of 10° are shown in Fig. 21(a). Clearly, an

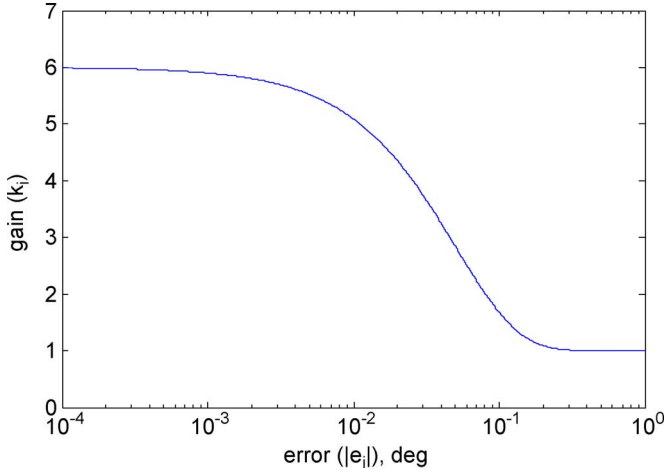


Fig. 19. CPP gain versus CPP error.

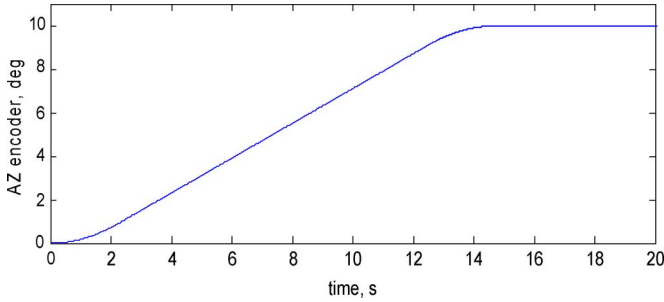


Fig. 20. CPP response to 10° step.

unstable limit cycling is present. The same response of the antenna with processed command is shown in Fig. 21(b), where the antenna follows closely the processed command, without limit-cycling.

VIII. POINTING ERROR SOURCES

The following is a list of the major pointing error sources, not detectable by the antenna sensors (encoders).

- The radio beam position is measured with a certain bias, since the encoders are not collocated with the beam.
- Only a certain portion of the disturbances can be compensated with the motors, since the antenna control torques are applied at the motor locations, while the wind disturbances are distributed over the antenna surface.
- Disturbances: Thermal and wind forces are the main sources of disturbances and are difficult to measure. Gravity forces and azimuth track imperfections are measurable and repeatable disturbances. Atmospheric refraction is a measurable but unrepeatable disturbance.
- Model uncertainty: Manufacturing imperfections and the variable antenna configuration (its structural properties depend on its elevation angle) are the sources of uncertainty that limit the controller performance.
- Nonlinearities: Backlash and friction torques at the antenna drives, rate, and acceleration limits are the main sources of nonlinearity.

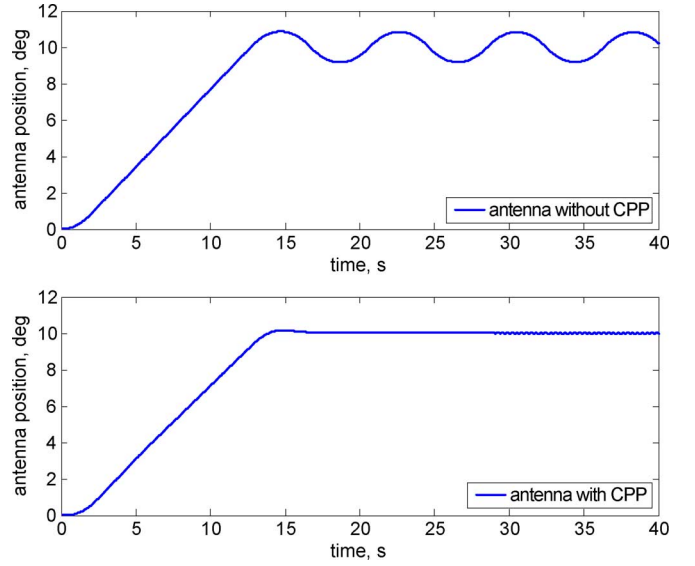


Fig. 21. Antenna response to 10° step: (a) without CPP and (b) with CPP.

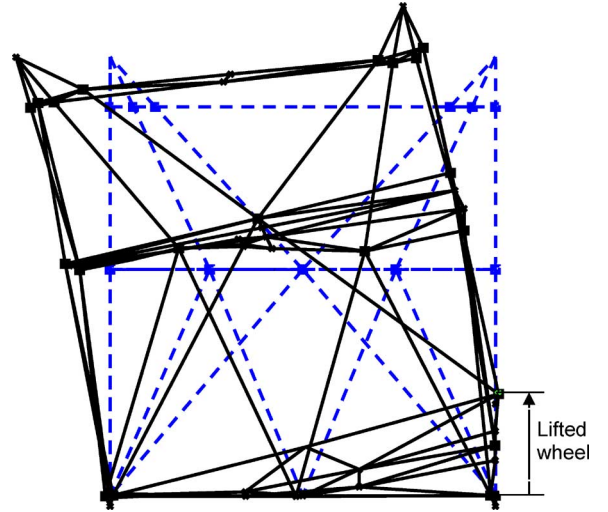


Fig. 22. Alidade deformation due to wheel lift.

The pointing error sources and the error corrections for the Green Bank telescope are presented in [47]; for active corrections of structural deformations see [48]; for tracking performance [49]; on use of inclinometers for measuring telescope position see [50]; on thermal and wind control of the Very Large Telescope (European Southern Observatory) see [51].

A. Azimuth Track Imperfections

Antennas rotate in azimuth on a circular azimuth track, which is manufactured with a level precision of ± 0.5 mm for the 34-m DSN antennas. On the azimuth track design, see [52]. The uneven azimuth track level causes antenna tilts and flexible deformations. The finite element model of the alidade (lower antenna structure) deformations due to track unevenness is shown in Fig. 22. Certainly, these deformations impact antenna pointing accuracy. However, the pointing errors caused by the track irregularities are repeatable, therefore, they can be calibrated. By developing a look-up table one provides pointing corrections as

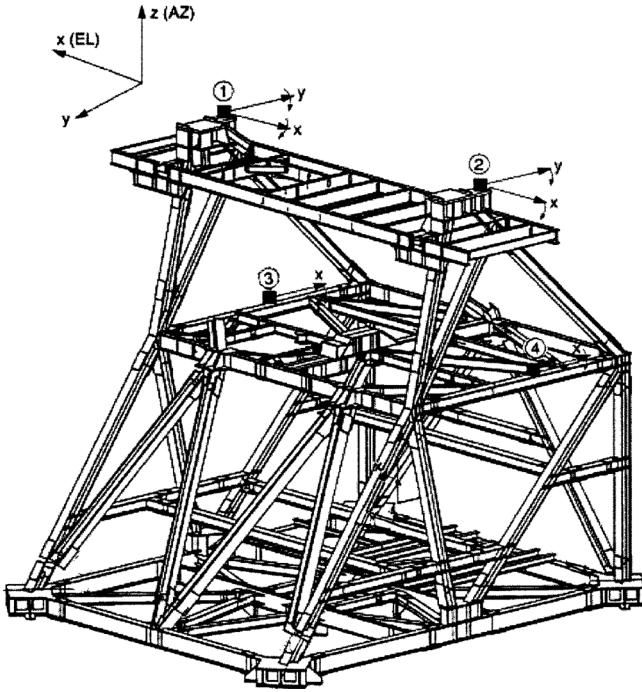


Fig. 23. Alidade and the inclinometer locations.

a function of the antenna azimuth position. The look-up table is generated by using inclinometers that measured tilts of the alidade structure at selected points.

Four inclinometers were installed on the alidade structure, at locations marked in Fig. 23. Each inclinometer measures tilts of its x - and y -axes. The locations of the inclinometers were selected such that their tilts estimate the alidade elevation and cross-elevation rotations at the antenna focal point. Inclinometers No. 1 and No. 2 are located at the top of the alidade. Inclinometer No. 2 is located next to the elevation encoder. The y -axis tilt of this inclinometer reflects the elevation pointing error. Inclinometers No. 3 and No. 4 are located in the middle of the crossbeam of the left and right sides of the alidade, respectively. Their x -axis tilts combined with the x -axis tilts of the inclinometers No. 1 and No. 2, give the cross-elevation pointing error, as shown in Fig. 23.

The x - and y -axis tilts of the i th inclinometer are denoted as α_{ix} and α_{iy} , respectively. The inclinometer data were collected during the antenna azimuth rotation at constant rate of 50 m°/s, and the sampling frequency of 2 Hz. The tests were performed during nighttime to minimize deformations of the antenna structure due to the thermal gradient. The data show satisfactory repeatability.

The antenna elevation error Δ_{el} is measured by the y tilt of the second inclinometer

$$\Delta_{el} = \alpha_{2y}. \quad (6)$$

The cross-elevation error (Δ_{xel}) depends on the antenna elevation position (θ) and on the rotation (δ_y) of the top of the alidade with respect to the y -axis (tilt of the elevation axis) and

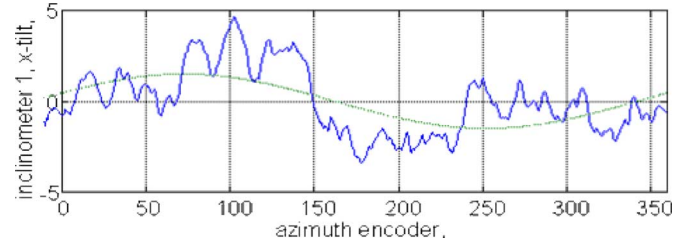
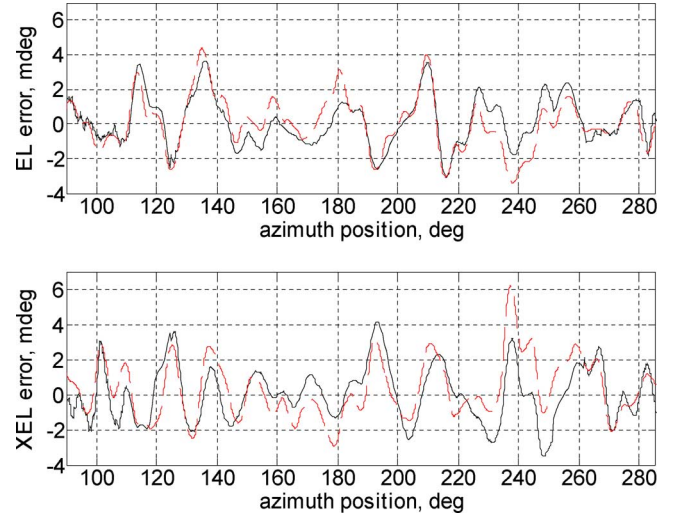
Fig. 24. Inclinometer No. 1 tilt, x -direction.

Fig. 25. Antenna pointing errors (EL—elevation, and XEL—cross-elevation) measured (black solid line) and predicted from the look-up table (red dashed line): (a) the elevation pointing error and (b) the cross-elevation pointing error.

the alidade twist δ_z (the rotation of the top of the alidade with respect to the z -axis)

$$\Delta_{xel} = \delta_z \cos(\theta) - \delta_y \sin(\theta). \quad (7)$$

The tilt of the elevation axis is an average of the x -tilts of the inclinometers 1 and 2, that is

$$\delta_y = 0.5(\alpha_{1x} + \alpha_{2x}) \quad (8)$$

while the alidade twist is determined from x tilts of the inclinometer No. 3 and No. 4

$$\delta_z = \frac{h}{l}(\alpha_{3x} - \alpha_{4x}) \quad (9)$$

where h is the alidade height and l is the distance between the inclinometers. The details are in [53].

The reading of the inclinometer 1, x -axis, is shown in Fig. 24. The fitted sinusoid shows the azimuth axis tilt. The pointing error obtained from the inclinometer measurements is shown in Fig. 25 (dashed line). The measurements of the actual pointing error (using the monopulse technique) are shown in the same figure by a solid line. The figure shows the coincidence of the inclinometer and the monopulse data.

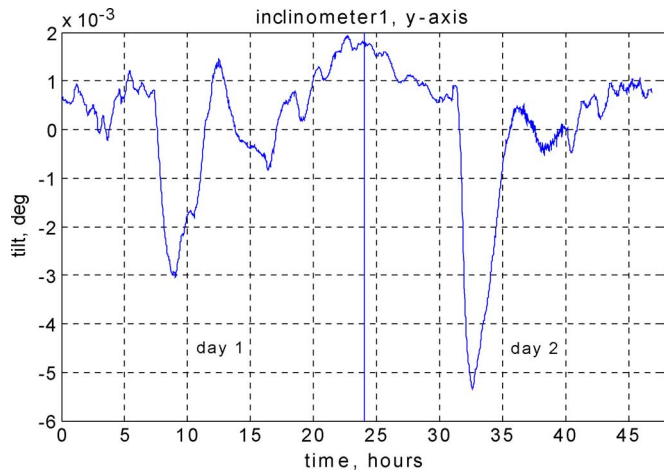


Fig. 26. Thermal deformations of the 34-m DSN antenna.

B. Thermal Deformations

The temperature gradient causes deformations of the antenna structure, thus, it impacts the pointing accuracy. The inclinometers were used to measure antenna tilts when it was stowed. A sample shown in Fig. 26 shows tilts of 8 m° . The largest tilts were in the afternoons, when the sun's heat was intensive (although the data were collected in November, which is not the hottest season at the Mojave Desert, where antennas are located). For techniques to compensate for the thermal deformations, see [51], [54], [55], and [56]. Many approaches prefer to control thermal environment of a telescope [57]–[62].

C. Gravity Deformations

Gravity forces deform antenna dish and subreflector, and the deformations depend on the dish elevation position. These deformations are repeatable and can be calculated comparatively accurately using the finite-element model. The gravity deformations of the 70-m antenna are shown in Fig. 27. The calculated deformations allow to generate a look-up table of the pointing corrections.

D. Atmospheric Refraction

The radio beam is bent while passing through the atmosphere, see Fig. 28. The amount of refraction depends on air humidity and can be calculated. The atmospheric conditions are monitored by weather stations, and the refraction model calculates the correction once every second. The refraction corrections are added to the antenna pointing model, and they can be of order of several hundred millidegrees.

E. Friction

Antenna/telescope drive friction can cause pointing errors. In order to improve pointing, the best thing is to reduce the friction. For example, the 70-m DSN antennas use oil film to rotate in azimuth. Machine jack-screws, often used in elevation drives, are sources of significant friction. When friction cannot be reduced through structural modifications, control engineering tools are implemented. One of them is dither, i.e., oscillations applied at the friction source to break the friction contact. The dither

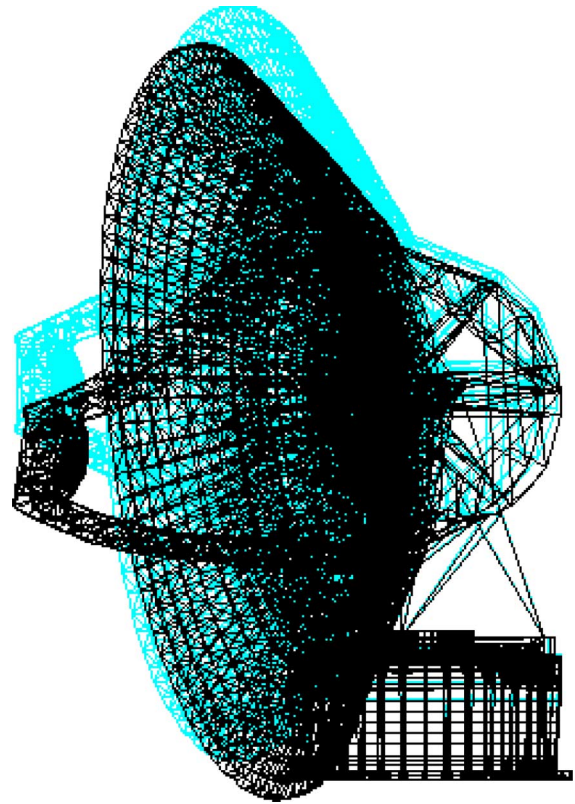


Fig. 27. Gravity deformation of the 70-m antenna.

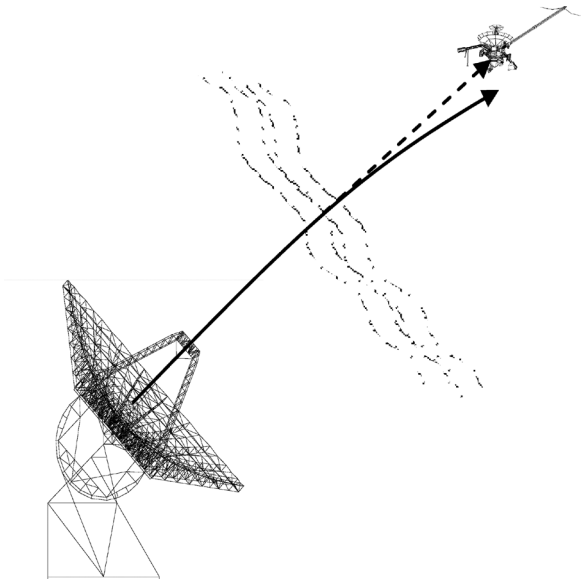


Fig. 28. Atmospheric refraction.

frequency shall be higher than the antenna structural frequencies, to avoid excitation of structural resonances. The analysis of dither as applied to the antenna is given in [63]. The friction modeling of the 2.5-m telescope is described in [64]. For more on friction compensation, see [65]–[67].

F. Backlash

Gearboxes and gears are antenna drive components. A backlash phenomenon at the gearboxes is observed when one gear

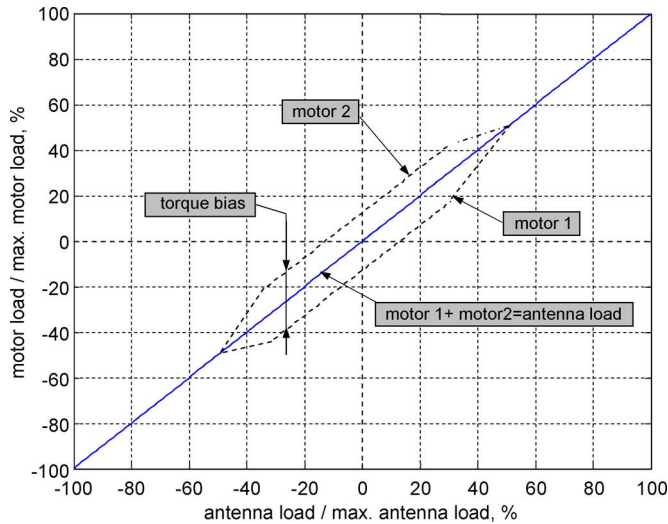


Fig. 29. Motor torques and the counter-torque.

rotates through a small angle without causing a corresponding movement of the second gear. This causes beating in the drives, gear wear, and deterioration of antenna tracking precision. In order to maintain antenna pointing precision, the backlash phenomenon is eliminated by implementing two symmetric drives with a specific torque difference between them, see Fig. 29. The torque difference is called a torque bias, or counter-torque. With two motor configurations the backlash clearance will occur at one drive while the other is still coupled. The antenna dynamics will be controlled by the latter drive. The effectiveness of the two-motor approach depends on the amount of torque bias applied at the drives, which depends on the antenna variable load (mainly wind). The torque bias should be large enough to lead the antenna through the gap for the maximal allowable torque load, but small enough that it will not cause excessive local stress, friction, or wear. For more information on backlash, see [68]–[75].

IX. POINTING ERROR CORRECTION

A. Look-up Tables

Look-up tables are used to correct for the known and repeatable errors (e.g., gravity deformations, azimuth track level corrections). For nonrepeatable errors, an additional feedback (e.g., conscan or monopulse) is applied.

B. Conical Scan (Conscan)

Conscan is an additional feedback. This technique is commonly used for the determination of the true spacecraft position. During conscan, circular movements are added to the antenna command as shown in Fig. 30. The circular movements cause sinusoidal variations of the power of the signal received from the spacecraft, as illustrated in Fig. 31. The power variations are used to estimate the true spacecraft position. The time of one cycle is between 30 and 60 s, thus, the correction update is comparatively slow. The drawback of this technique is that the antenna is always off the peak power, i.e., always slightly off the target.

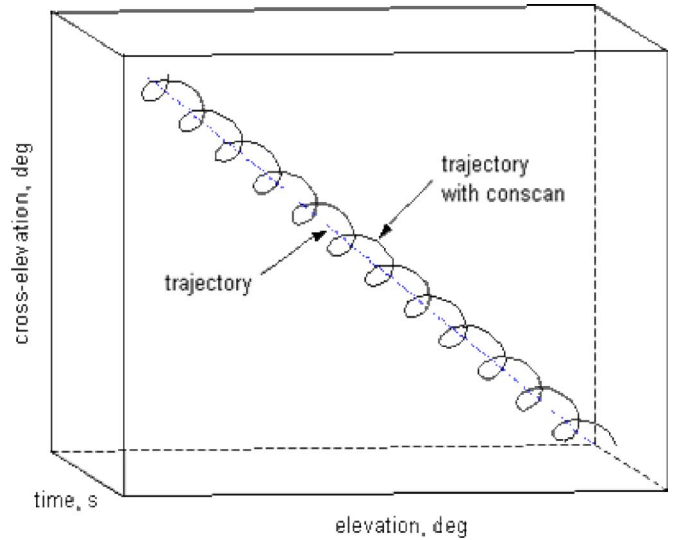


Fig. 30. Antenna trajectory when performing conical scan.

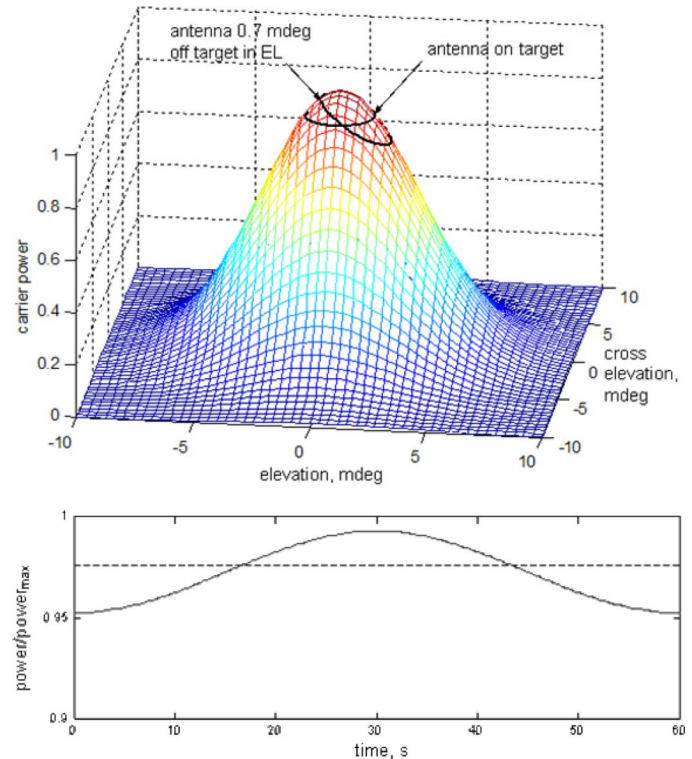


Fig. 31. Antenna power variation during conscan.

The control system of the conscan consists of the additional (outer) feedback that corrects for the difference between encoder and radio beam position, see Fig. 32. For more about conscan, see [76] and [77].

C. Monopulse

In this algorithm, the pointing error is estimated from radio beam received by the monopulse feed-horns. The horns are slightly displaced so that they receive the signal from a slightly different angle. These signals are added and subtracted. The sum represents the power of the signal, the difference represents the beam error (when antenna points with zero error, the differ-

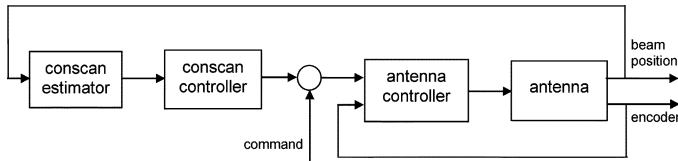


Fig. 32. Antenna conscan controller.

ence is zero). If the difference is non-zero, the deviation is used to estimate the pointing error. The process is conducted in two dimensions (elevation and cross-elevation angle). The recent monopulse technique, a single monopulse feed, allows direct pointing at the target at all times, allowing for the spacecraft to be tracked at the peak of the antenna pattern. This technique is much faster than conscan (updating time is 0.02 s). For more about monopulse, see [6], [78], and [79].

X. CONCLUSIONS

The purpose of this paper was to collect and evaluate the challenges that control system engineers encounter while trying to satisfy the demanding pointing requirements. Not all challenges have satisfactory solutions.

The paper showed that control and pointing challenges are not exactly the same. The antenna control system is designed to minimize the servo error, a difference between the command and the antenna position as sensed by encoders. Even if the servo error is virtually zero, the pointing might be (and in most cases, is) unacceptable. It is because the encoders do not measure the actual orientation of the beam. The encoders are not collocated with the beam, and structural compliance, thermal deformations, etc., create the discrepancy between encoder reading and the beam position. Therefore, improvement of the control system is tied to the improvement of the pointing accuracy: there is no reason to reduce the controller servo error if the errors caused by pointing imperfection exceed it significantly.

Finally, the future telescope projects, such as TMT [14], GMT [80], CELT [81]–[83], OWL [84], Euro50 [85], or the Chinese Future Giant Telescope [86] with the stringent pointing requirements, work on development of sensors that do not distinguish between disturbances caused by atmosphere, antenna structure, and antenna environment, and develop actuators that can correct the sensed antenna performance.

ACKNOWLEDGMENT

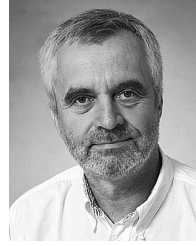
Many individuals have made contributions of great value to this paper. The co-workers: F. Baher, H. Ahlstrom, M. Gudim, W. Hurt, J. Mellstrom, C. Racho, A. Bernardo, and B. Parvin in the azimuth track level analysis and measurements, controller testing, system identification, friction analysis, monopulse analysis, and testing; W. Almassy, of Honeywell in the command preprocessor development and testing; K. Souccar of LMT in the LMT control design; B. Bienkiewicz of Colorado State University in wind modeling. Also, former students E. Maneri of Montana State University, in the controller GUI development and the backlash analysis, J. Brandt of University of Washington, in backlash modeling, and E. Craparo of Massachusetts Institute of Technology in conscan analysis.

REFERENCES

- [1] Jet Propulsion Laboratory, "The Interplanetary Network Progress Report," Pasadena, CA [Online]. Available: <http://ipnpr.jpl.nasa.gov/index.cfm>
- [2] T. Kitsuregawa, *Advanced Technology in Satellite Communication Antennas: Electrical and Mechanical Design*. Norwood, MA: Artech House, 1990.
- [3] R. Levy, *Structural Engineering of Microwave Antennas*. Piscataway, NJ: IEEE Press, 1996.
- [4] G. Biernson, *Optimal Radar Tracking Systems*. New York: Wiley-Intersci., 1990.
- [5] W. Gawronski, *Advanced Structural Dynamics, and Active Control of Structures*. New York: Springer-Verlag, 2004.
- [6] J. C. Toomay, *Radar Principles for the Non-Specialist*. New York: Van Nostrand, 1989.
- [7] T. Macnamara, *Handbook of Antennas for EMC*. Norwood, MA: Artech House, 1995.
- [8] W. Gawronski and J. A. Mellstrom, "Control and dynamics of the deep space network antennas," in *Control and Dynamic Systems*. San Diego, CA: Academic, 1994, vol. 63.
- [9] NASA, Jet Propulsion Lab., California Inst. Technol., Pasadena, CA, "The NASA deep space network," 2006 [Online]. Available: deepspace.jpl.nasa.gov/dsn/
- [10] "The large millimeter telescope project," Pasadena, CA, 2005 [Online]. Available: www.lmtgtm.org/
- [11] Max-Planck-Institut Radioastronomie, Bonn, Germany, "APEX, the atacama pathfinder experiment," 2006 [Online]. Available: <http://www.apex-telescope.org/>
- [12] ESA European Space Operations Centre, Darmstadt, Germany, "Ground stations," 2006 [Online]. Available: http://www.esa.int/SPECIALS/ESOC/SEMZEEW4QWD_0.html
- [13] ALMA, Atacama Desert, Chile, "The Atacama large millimeter array," 2005 [Online]. Available: www.alma.nrao.edu/info
- [14] AURA, "The thirty meter telescope project," 2001 [Online]. Available: tmt.ucolick.org/
- [15] MMT Observatory, Tucson, AZ, "The multiple mirror telescope," 2006 [Online]. Available: www.mmto.org/
- [16] W. Gawronski and K. Souccar, "Control system of the large millimeter telescope," in *Proc. SPIE Astronom. Telescopes Instrumentation Conf.*, 2004, pp. 104–115.
- [17] D. Clark, "Control system prototyping—A case study," Tech. Memo. ITM-04-3, 2004 [Online]. Available: www.mmto.org/MMTpapers/tech00_10.shtml#2004
- [18] T. Erm and P. Gutierrez, "Integration and tuning of the VLT drive systems," in *Proc. SPIE Telescope Structures, Enclosures, Contr., Assembly/Integr./Validation Commissioning*, 2000, pp. 490–499.
- [19] S. Jimenez-Garcia, M. E. Magana, J. S. Benitez-Read, and J. Martinez-Carbalido, "Modeling, simulation, and gain scheduling control of large radiotelescopes," *Simulation Practice Theory*, vol. 8, pp. 141–160, 2000.
- [20] W. Gawronski, C. Racho, and J. Mellstrom, "Application of the LQG and feedforward controllers for the DSN antennas," *IEEE Trans. Contr. Syst. Technol.* vol. 3, no. 4, pp. 417–421, Nov. 1995.
- [21] W. Gawronski, H. G. Ahlstrom, and A. M. Bernardo, "Analysis and performance of the control systems of the NASA 70-meter antennas," *ISA Trans.* pp. 490–499, 2004.
- [22] D. Clark, "Selected results of recent MMT servo testing," Tech. Memo. ITM-03-5, 2003 [Online]. Available: www.mmto.org/MMTpapers/pdfs/itm/itm03-5.pdf
- [23] E. Cascone, D. Mancini, and P. Schipani, "Galileo telescope model identification," *Proc. SPIE*, vol. 3112, pp. 343–350, 1997.
- [24] E. Simiu and R. H. Scanlan, *Wind Effects on Structures*. New York: Wiley, 1978.
- [25] W. Gawronski and W. Almassy, "Command pre-processor for radiotelescopes and microwave antennas," *IEEE Antennas Propag. Mag.* vol. 44, no. 2, pp. 30–37, Apr. 2002.
- [26] W. Gawronski, B. Bienkiewicz, and R. E. Hill, "Wind-induced dynamics of a deep space network antenna," *J. Sound Vibration*, vol. 178, no. 1, pp. 67–77, 1994.
- [27] W. Gawronski, "Modeling wind gusts disturbances for the analysis of antenna pointing accuracy," *IEEE Antennas Propag. Mag.* vol. 46, no. 1, pp. 50–58, Feb. 2004.
- [28] G. Z. Angeli, M. K. Cho, M. Sheehan, and L. M. Stepp, "Characterization of wind loading of telescopes," in *Proc. SPIE, Integr. Modeling Telescopes*, 2002, pp. 72–83.

- [29] W. Gawronski, J. Mellstrom, and B. Bienkiewicz, "Antenna mean wind torques: A comparison of field and wind tunnel data," *IEEE Antennas Propag. Mag.*, vol. 47, no. 5, pp. 55–59, Oct. 2005.
- [30] J. Mann, "Wind field simulations," *Prob. Eng. Mech.*, vol. 13, pp. 269–282, 1998.
- [31] W. Gawronski, "Predictive controller and estimator for NASA deep space network antennas," *ASME Trans., J. Dyn. Syst., Meas., Contr.* no. 2, pp. 241–248, 1994.
- [32] T. Erm and S. Sandrock, "Adaptive periodic error correction for the VLT telescopes," in *Proc. SPIE Large Ground-Based Telescopes*, 2002, pp. 900–909.
- [33] D. Mancini, M. Brescia, E. Cascote, and P. Schipani, "A variable structure control law for telescopes pointing and tracking," *Proc. SPIE*, vol. 3086, pp. 72–84, 1997.
- [34] W. Gawronski, "Antenna control systems: From PI to H_∞ ," *IEEE Antennas Propag. Mag.*, vol. 43, no. 1, pp. 52–60, Feb. 2001.
- [35] —, "Antenna linear quadratic gaussian (LQG) controllers: Properties, limits of performance, and tuning procedure," in *Proc. 16th IFAC Congress*, 2005, pp. 2251–2257.
- [36] E. Maneri and W. Gawronski, "LQG controller design using GUI: Application to antennas and radio-telescopes," *ISA Trans.* vol. 39, pp. 243–264, 2000.
- [37] M. Olberg, C. Lindeborg, A. Seyf, and C. F. Kastengren, "A simple robust digital controller for the oncala 20 m radio telescope," *Proc. SPIE*, vol. 2479, pp. 257–265, 1995.
- [38] W. Gawronski, " H_∞ controller for the DSS13 antenna with wind disturbance rejection properties," TDA Progress Rep. 42–127, 1996 [Online]. Available: tmo.jpl.nasa.gov/tmo/progress_report/42-127/127G.pdf
- [39] U. Schoenhoff, A. Klein, and R. Nordmann, "Attitude control of the airborne telescope SOFIA: μ -synthesis for a large scaled flexible structure," in *Proc. 39th IEEE Conf. Dec. Contr.*, 2000, pp. 3576–3581.
- [40] T. Erm, B. Bauvir, and Z. Hurak, "Time to go H-infinity?," in *Proc. SPIE, Adv. Softw., Contr., Commun. Syst. Astronomy*, 2004, pp. 68–78.
- [41] K. Li, E. B. Kosmatopoulos, P. A. Ioannou, and H. Ryciotaki-Bousalis, "Large segmented telescopes: centralized, decentralized and overlapping control designs," *IEEE Contr. Syst. Mag.*, vol. 20, no. 5, pp. 59–72, Oct. 2000.
- [42] K. Li, E. B. Kosmatopoulos, P. A. Ioannou, H. Boussalis, and A. Chasiakos, "Control techniques for a large segmented reflector," in *Proc. 37th IEEE Conf. Dec. Contr.*, 1998, pp. 813–818.
- [43] M. Whorton and G. Angeli, "Modern control for the secondary mirror of a giant segmented mirror telescope," *Proc. SPIE, Future Giant Telescopes*, vol. 4840, pp. 140–150, 2003.
- [44] Y. Peng, D. Vrancic, and R. Hanus, "Anti-windup, bumpless, and conditioned transfer techniques for PID controllers," *IEEE Contr. Syst. Mag.*, vol. 16, no. 4, pp. 48–57, Aug. 1996.
- [45] D. Mancini, M. Brescia, E. Cascote, and P. Schipani, "A neural variable structure controller for telescopes pointing and tracking improvement," *Proc. SPIE*, vol. 3112, pp. 335–342, 1997.
- [46] S. R. Tyler, "A trajectory preprocessor for antenna pointing," Tech. TDA Progress Rep. 42-118, 1994 [Online]. Available: tmo.jpl.nasa.gov/tmo/progress_report/42-118/118E.pdf
- [47] J. J. Brandt, "Controlling the green bank telescope," *Proc. SPIE, Adv. Telescope Instrumentation Contr. Softw.*, vol. 4009, pp. 96–108, 2000.
- [48] H. Baier and G. Locatelli, "Active and passive microvibration control in telescope structures," *Proc. SPIE, Telescope Structures, Enclosures, Contr., Assembly/Integr./Validation Commissioning*, vol. 4004, pp. 267–276, 2000.
- [49] T. Erm, "Analysis of tracking performance," in *Proc. SPIE, Opt. Telescopes Today Tomorrow*, 1996, vol. 2871, pp. 1032–1040.
- [50] R. Kibrick, L. Robinson, V. Wallace, and D. Cowley, "Tests of a precision tiltmeter system for measuring telescope position," *Proc. SPIE*, vol. 3351, pp. 342–353, 1998.
- [51] M. Cullum and J. Spyromilio, "Thermal and wind control of the VLT," in *Proc. SPIE, Telescope Structures, Enclosures, Contr., Assembly/Integr./Validation Commissioning*, 2000, vol. 4004, pp. 194–201.
- [52] J. Antebi and F. W. Kan, "Precision continuous high-strength azimuth track for large telescopes," in *Proc. SPIE, Future Giant Telescopes*, 2003, vol. 4840, pp. 612–623.
- [53] W. Gawronski, F. Baher, and O. Quintero, "Azimuth track level compensation to reduce blind pointing errors of the deep space network antennas," *IEEE Antennas Propag. Mag.* vol. 42, no. 2, pp. 28–38, Apr. 2000.
- [54] A. Greve, M. Dan, and J. Penalver, "Thermal behavior of millimeter wavelength radio telescopes," *IEEE Trans. Antennas Propag. Mag.*, vol. 40, no. 11, pp. 1375–1388, Nov. 1992.
- [55] A. Greve and G. MacLeod, "Thermal model calculations of enclosures for millimeter wavelength radio telescopes," *Radio Science*, vol. 36, no. 5, pp. 1111–1128, 2001.
- [56] J. W. M. Baars, A. Greve, B. G. Hooghoudt, and J. Penalver, "Thermal control of the IRAM 30-m millimeter radio telescope," *Astronomy Astrophys.*, vol. 195, pp. 364–371, 1988.
- [57] G. G. Williams, J. D. Gibson, S. Callahan, D. Blanco, J. T. Williams, and P. Spencer, "Performance and control of the MMT thermal system," in *Proc. SPIE, Ground-Based Telescopes*, 2004, vol. 5489, pp. 938–949.
- [58] H. J. Kaercher and J. W. M. Baars, "The design of the Large Millimeter Telescope/Gran Telescopio Milimetrico (LMT/GTM)," in *Proc. SPIE, Radio Telescopes*, 2000, vol. 4015, pp. 155–168.
- [59] G. Talbot, D. Abrams, C. Benn, A. Chopping, K. Dec, S. Els, M. Fisher, S. Goodsell, D. Gray, and P. Jolley, "GRACE: A controlled environment for adaptive optics at the William Herschel Telescope," in *Proc. SPIE, Adv. Adaptive Opt.*, 2004, vol. 5490, pp. 462–472.
- [60] R. Brunswick, "Development and testing of a unique telescope enclosure design, optimized for seeing and telescope thermal control," in *Proc. SPIE, Astronom. Structures Mech. Technol.*, 2004, vol. 5495, pp. 565–576.
- [61] A. Miyashita, R. Ogasawara, N. Takato, G. Kosugi, T. Takata, and F. Uruguchi, "Temperature control for the primary mirror and seeing statistics of Subaru telescope," in *Proc. SPIE, Large Ground-Based Telescopes*, 2003, vol. 4837, pp. 255–263.
- [62] A. Greve, M. Bremer, J. Penalver, P. Raffin, and D. Morris, "Improvement of the IRAM 30-m telescope from temperature measurements and finite-element calculations," *IEEE Trans. Antennas Propag. Mag.*, vol. 53, no. 2, pp. 851–860, Feb. 2005.
- [63] W. Gawronski and B. Parvin, "Radiotelescope low rate tracking using dither," *AIAA J. Guid., Contr., Dyn.*, vol. 21, pp. 349–352, 1998.
- [64] C. H. Rivetta and S. Hansen, "Friction model of the 2.5 mts SDSS telescope," *Proc. SPIE*, vol. 3351, pp. 466–477, 1998.
- [65] A. Ramasubramanian and L. R. Ray, "Adaptive friction compensation using extended Kalman-Bucy filter friction estimation: A comparative study," in *Proc. Amer. Contr. Conf.*, 2000, pp. 2588–2594.
- [66] J. Moreno, R. Kelly, and R. Campa, "On velocity control using friction compensation," in *Proc. 41st Conf. Dec. Contr.*, 2002, pp. 95–100.
- [67] M. Feemster, P. Vedagarbha, D. M. Dawson, and D. Haste, "Adaptive control techniques for friction compensation," in *Proc. Amer. Contr. Conf.*, 1998, pp. 1488–1492.
- [68] M. Nordin and P. O. Gutman, "Controlling mechanical systems with backlash—A survey," *Automatica*, vol. 38, pp. 1633–1649, 2002.
- [69] R. Dhaoui, K. Kubo, and M. Tobise, "Analysis and compensation of speed drive system with torsional loads," *IEEE Trans. Ind. Appl.*, vol. 30, no. 3, pp. 760–766, May/Jun. 1994.
- [70] M. T. Mata-Jimenez, B. Brogliato, and A. Goswami, "On the control of mechanical systems with dynamics backlash," in *Proc. 36th Conf. Dec. Contr.*, 1997, pp. 1990–1995.
- [71] B. Friedland, "Feedback control of systems with parasitic effects," in *Proc. Amer. Contr. Conf.*, 1997, pp. 937–941.
- [72] J. L. Stein and C.-H. Wang, "Estimation of gear backlash: Theory and simulation," *J. Dyn. Syst., Meas., Contr.*, vol. 120, pp. 74–82, 1998.
- [73] N. Sarkar, R. E. Ellis, and T. N. Moore, "Backlash detection in geared mechanisms: modeling, simulation, and experimentation," *Mech. Syst. Signal Process.*, vol. 11, no. 3, pp. 391–408, 1997.
- [74] A. A. Stark, R. A. Chamberlin, J. G. Ingalls, J. Cheng, and G. Wright, "Optical and mechanical design of the antarctic submillimeter telescope and remote observatory," *Rev. Sci. Instrum.*, vol. 68, no. 5, pp. 2200–2213, 1997.
- [75] W. Gawronski, J. J. Brandt, H. G. Ahlstrom, Jr., and E. Maneri, "Torque bias profile for improved tracking of the deep space network antennas," *IEEE Antennas Propag. Mag.* vol. 42, no. 6, pp. 35–45, Dec. 2000.
- [76] W. Gawronski and E. Craparo, "Antenna scanning techniques for estimation of spacecraft position," *IEEE Antennas Propag. Mag.* vol. 44, no. 6, pp. 38–45, Dec. 2002.
- [77] N. Levanon, "Upgrading conical scan with off-boresight measurements," *IEEE Trans. Aerosp. Electron. Syst.*, vol. 33, no. 4, pp. 1350–1357, Oct. 1997.
- [78] M. A. Gudim, W. Gawronski, W. J. Hurd, P. R. Brown, and D. M. Strain, "Design and performance of the monopulse pointing system of the DSN 34-meter beam-waveguide antennas," TMO PR 42-138, 1999.
- [79] W. Gawronski and M. A. Gudim, "Design and performance of the monopulse control system," *IEEE Antennas Propag. Mag.* vol. 41, no. 6, pp. 40–50, Dec. 1999.

- [80] S. Gunnels, W. Davison, B. Cuerden, and E. Hertz, "The Giant Magellan Telescope (GMT) structure," in *Proc. SPIE, Astronomical Structures Mech. Technol.*, 2004, vol. 5495, pp. 168–179.
- [81] J. Nelson, "Progress on the California Extremely Large Telescope (CELT)," in *Proc. SPIE, Future Giant Telescopes*, 2003, vol. 4840, pp. 47–59.
- [82] S. E. Strom, L. Stepp, and B. Gregory, "Giant segmented mirror telescope: A point design based on science drivers," in *Proc. SPIE, Future Giant Telescopes*, 2003, vol. 4840, pp. 116–128.
- [83] G. Z. Angeli, M. K. Cho, and M. S. Whorton, "Active optics and control architecture for a giant segmented mirror telescope," in *Proc. SPIE, Future Giant Telescopes*, 2003, vol. 4840, pp. 129–139.
- [84] P. Dierickx, J. L. Beckers, E. Brunetto, R. Conan, E. Fedrigo, R. Gilmozzi, N. Hubin, F. Koch, M. Le Louarn, E. Marchetti, G. Monnet, L. Noethe, M. Quattri, M. Sarazin, J. Spyromilio, and N. Yaitskova, "The eye on the beholder: Designing the OWL," in *Proc. SPIE, Future Giant Telescopes*, 2003, vol. 4840, pp. 151–170.
- [85] T. Andersen, A. Ardeberg, J. Beckers, A. Goncharov, M. Owner-Petersen, H. Riewaldi, R. Snel, and D. Walker, "The Euro50 extremely large telescope," in *Proc. SPIE, Future Giant Telescopes*, 2003, vol. 4840, pp. 214–225.
- [86] G. Li and D. Yang, "Preliminary structure design and analysis of the chinese future giant telescope," in *Proc. SPIE, Astronomical Structures Mech. Technol.*, 2004, vol. 5495, pp. 204–215.



Wodek Gawronski received the M.Sc. and Ph.D. degrees in mechanical engineering from the Technical University of Gdansk, Gdansk, Poland, in 1968 and 1971, respectively.

Currently, he is an Engineering Principal at the Communication Ground Systems Section, Jet Propulsion Laboratory, Pasadena, CA, where he is responsible for the control system analysis and design of the NASA Deep Space Network antennas. He was a Professor of dynamics and controls at the Technical University of Gdansk and at the University

of Hanover, Hanover, Germany. Later, he was a NRC Senior Fellow at the NASA Langley Research Center, Hampton, VA, where he worked on spacecraft structural dynamics and controls problems. He was also a Consultant on control system design to several radiotelescope projects, including the NRAO 100-m Green Bank Telescope, West Virginia, and the 50-m Large Millimeter Wavelength Telescope in Pueblo, Mexico.

Dr. Gawronski is also an Associate Editor of the *AIAA Journal of Guidance Control and Dynamics*.